

Flow Sensor Test Article (F-STAr) – Assembly and Water Testing Report

Nuclear Science and Engineering Division

About Argonne National Laboratory

Argonne is a U.S. Department of Energy laboratory managed by UChicago Argonne, LLC under contract DE-AC02-06CH11357. The Laboratory's main facility is outside Chicago, at 9700 South Cass Avenue, Argonne, Illinois 60439. For information about Argonne and its pioneering science and technology programs, see <http://www.anl.gov>.

DOCUMENT AVAILABILITY

Online Access: U.S. Department of Energy (DOE) reports produced after 1991 and a growing number of pre-1991 documents are available free at OSTI.GOV (<http://www.osti.gov/>), a service of the US Dept. of Energy's Office of Scientific and Technical Information.

Reports not in digital format may be purchased by the public from the National Technical Information Service (NTIS):

U.S. Department of Commerce
National Technical Information Service
5301 Shawnee Rd
Alexandra, VA 22312
www.ntis.gov
Phone: (800) 553-NTIS (6847) or (703) 605-6000
Fax: (703) 605-6900
Email: orders@ntis.gov

Reports not in digital format are available to DOE and DOE contractors from the Office of Scientific and Technical Information (OSTI):

U.S. Department of Energy
Office of Scientific and Technical Information
P.O. Box 62
Oak Ridge, TN 37831-0062
www.osti.gov
Phone: (865) 576-8401
Fax: (865) 576-5728
Email: reports@osti.gov

Disclaimer

This report was prepared as an account of work sponsored by an agency of the United States Government. Neither the United States Government nor any agency thereof, nor UChicago Argonne, LLC, nor any of their employees or officers, makes any warranty, express or implied, or assumes any legal liability or responsibility for the accuracy, completeness, or usefulness of any information, apparatus, product, or process disclosed, or represents that its use would not infringe privately owned rights. Reference herein to any specific commercial product, process, or service by trade name, trademark, manufacturer, or otherwise, does not necessarily constitute or imply its endorsement, recommendation, or favoring by the United States Government or any agency thereof. The views and opinions of document authors expressed herein do not necessarily state or reflect those of the United States Government or any agency thereof, Argonne National Laboratory, or UChicago Argonne, LLC

Flow Sensor Test Article (F-STAr) – Assembly and Water Testing Report

J. Rein, M. Weathered, E. Kent, D. Kultgen, A. Grannan, E. Ogren, C. Grandy

Nuclear Science and Engineering Division
Argonne National Laboratory

August 2023

Errata

After initial publication of this report the authors were made aware of some minor errors. These errors have been corrected in the present version.

Location	Error	Correction
Page 1, Section 1, Paragraph 2	Paragraph refers to an outdated Figure 1.	Updated Figure 1 description to reflect the updated figure.
Page 2, Section 1, Figure 2	Outdated figure showing two Fluidic Diode configurations.	Added an updated figure showing three different configurations, including a Fluidic Diode, Temperature Dependent Orifice, and Heat Exchanger.
Page 14, Section 3.5, Figure 19	Outdated photo of the submersible EMFM.	Added an updated photo of the submersible EMFM.
Page 16, Section 4.1, Paragraph 1	No explanation of why de-ionized water was used during water commissioning.	Reworked this paragraph to provide more detail on the water system, to better explain how the system works, and to explain why de-ionized water was needed during water commissioning.
Page 23, Section 5.4.1, Paragraph 2	No explanation of what axis the Pump Speed should be referenced to.	Added an explanation that the Pump Speed should be referenced on the left vertical axis.
Page 23, Section 5.4.1, Figure 26	Pump Speed legend label, left vertical axis label, and caption.	Changed the legend label from “Signal” to “Normalized Signal” and changed the vertical axis label from “Normalized Signal Difference [%]” to “[%]”. Added in the caption an explanation of what axis the pump speed is reference to.
Page 24, Section 5.4.2	No interpretation and discussion of the calibration curve.	Added third paragraph on Page 24 providing interpretation of calibration curve and a discussion of extrapolation.

Contents

1	Executive Summary	1
2	Introduction.....	3
3	Fabrication and Assembly.....	3
3.1	Main Flange and Baffle Plate	5
3.2	Pump.....	7
3.3	Support Structure, UIS Baffle Plating, and Test Section.....	8
3.4	Heater and Cooler.....	12
3.5	Flowmeter.....	13
3.6	Power Distribution, Data and Control Systems	15
4	Initial Water Testing	16
4.1	Water System and Setup.....	16
4.2	Water Testing and System Loss Curves	18
5	Flowmeter Calibration	19
5.1	Methodology.....	19
5.2	Uncertainty Analysis	20
5.2.1	Uncertainty Budget	20
5.2.2	EMFM Calibration Uncertainty	21
5.3	Experimental Setup	22
5.4	Calibration	23
5.4.1	Conduit Wall Wetting	23
5.4.2	Calibration Curves	24
5.4.3	Error Estimate	26
6	Conclusions and Path Forward	27
7	Acknowledgements.....	28
8	References.....	29

List of Figures

Figure 1 – A model view on the left and a photo of the F-STAr mock-up on the right. Note that the submersible flowmeter is not installed in the mock-up view.....	1
Figure 2 – Three concept views of hypothetical F-STAr configurations. Configurations shown are: a Fluidic Diode (left); a Temperature Dependent Orifice (center); and a heat exchanger (right).....	2
Figure 3 –A simplified P&ID diagram of F-STAr on the left. A model view of F-STAr annotated with the main components on the right.....	4
Figure 4 – Mock-up of F-STAr prior to water testing in the B206 Hi-Bay. Note that the F-STAr Submersible EMFM is not installed.	4
Figure 5 – Top-down view of the F-STAr main flange mounted to the A-Frame flipper.	5
Figure 6 – Top-down view of the baffle plate used to reduce churning and splashing at the sodium surface.	6
Figure 7 – Bottom-up view of the baffle plate used to reduce churning and splashing at the sodium surface.	6
Figure 8 – F-STAr pump installed onto the main flange.	7
Figure 9 – Modified pump volute and inlet bell. Originally, the volute was designed to use NPT fittings. However, these were removed to avoid potential seizing during assembly and disassembly after sodium service.	8
Figure 10 – Assembled Full-Scaled Test Section stack-up.....	9
Figure 11 – Full-Scaled Test Section installed into the support structure stack-up.....	9
Figure 12 – View looking down the rabbit tube positioner and into the Full-Scaled Test Section flow conditioner.	10
Figure 13 – Close-up view of test section baffle plate. This piece also doubles as a piece used to position the rabbit tube relative to the test section.....	10
Figure 14 – Rabbit Tube positioned near Full-Scaled Test Section.....	11
Figure 15 – Photo of immersion heater.....	12
Figure 16 – Photo of the U-Tube immersion cooler.	12
Figure 17 – Top-down view of the completed submersible EMFM magnet yoke.	13
Figure 18 – FEA model of the centerline magnetic field as a function of magnet height plotted with a single experimental measurement.	13
Figure 19 – Completed F-STAr submersible EMFM.	14
Figure 20 – 480 VAC Power Distribution (left), Data Acquisition and Control (center), and Heater Controller (right) enclosures setup on a temporary frame.	15
Figure 21 – Water Fill and Purification system used to fill the water testing tank on the left.....	16
Figure 22 – Setup used for water qualification testing of F-STAr. Note that this setup uses a turbine water flowmeter and significantly more piping than the sodium setup, meaning that pressure losses in this configuration were assumed to be higher than those in the sodium configuration.....	17
Figure 23 - F-STAr system loss curves plotted with estimated pump curves derived from THETA's pump using affinity laws.....	18

Figure 24 – F-STAr submersible EMFM calibration setup model.	19
Figure 25 – Experimental setup for sodium calibration of the F-STAr EMFM.	22
Figure 26 – Normalized EMFM signal, pump speed, sodium temperature, and magnet temperature over an elapsed time of 20-hrs. Note that the normalized signal and pump speed are both referenced on the left axis. After an initial wetting phase over the first two hours of testing, the EMFM signal reached an asymptotic value.....	23
Figure 27 – Flowmeter calibration curves at 200-C and 400-C.....	24
Figure 28 – Calibration coefficient calculated using Equation 5 with error bars.....	25
Figure 29 – Estimated F-STAr EMFM error at 200-C and 400-C. Note that the calculated difference between the F-STAr EMFM and reference flowmeter is bounded by the theoretically calculated calibration coefficient error.....	26

List of Tables

Table 1 – Budget of estimated uncertainties of the measured variables during calibration of the F-STAr reference flowmeter.	20
Table 2 – Accuracy of the vortex shedding flowmeter. The flowrates were calculated using a 1.63-inch inner diameter with sodium properties evaluated using Fink.	21
Table 3 – Coefficients and standard errors of Equation 12.....	25

1 Executive Summary

The Flow Sensor Test Article (F-STAr) is a new test article under development for the Mechanisms Engineering Test Loop (METL) facility at Argonne National Laboratory. F-STAr's purpose is to provide sodium submersible, high flowrate testing capabilities for the development of sensors, components, fluid studies and more. Figure 1 shows a model view on the left and a photo of the F-STAr mock-up on the right. Both views are annotated with the test articles main components, which include a high-capacity pump that is expected to provide a nominal flowrate of 120 GPM; a test section support structure that can accommodate a wide array of sub-test articles and their instrumentation; and finally, a heating and cooling system to aid in controlling the testing environment.

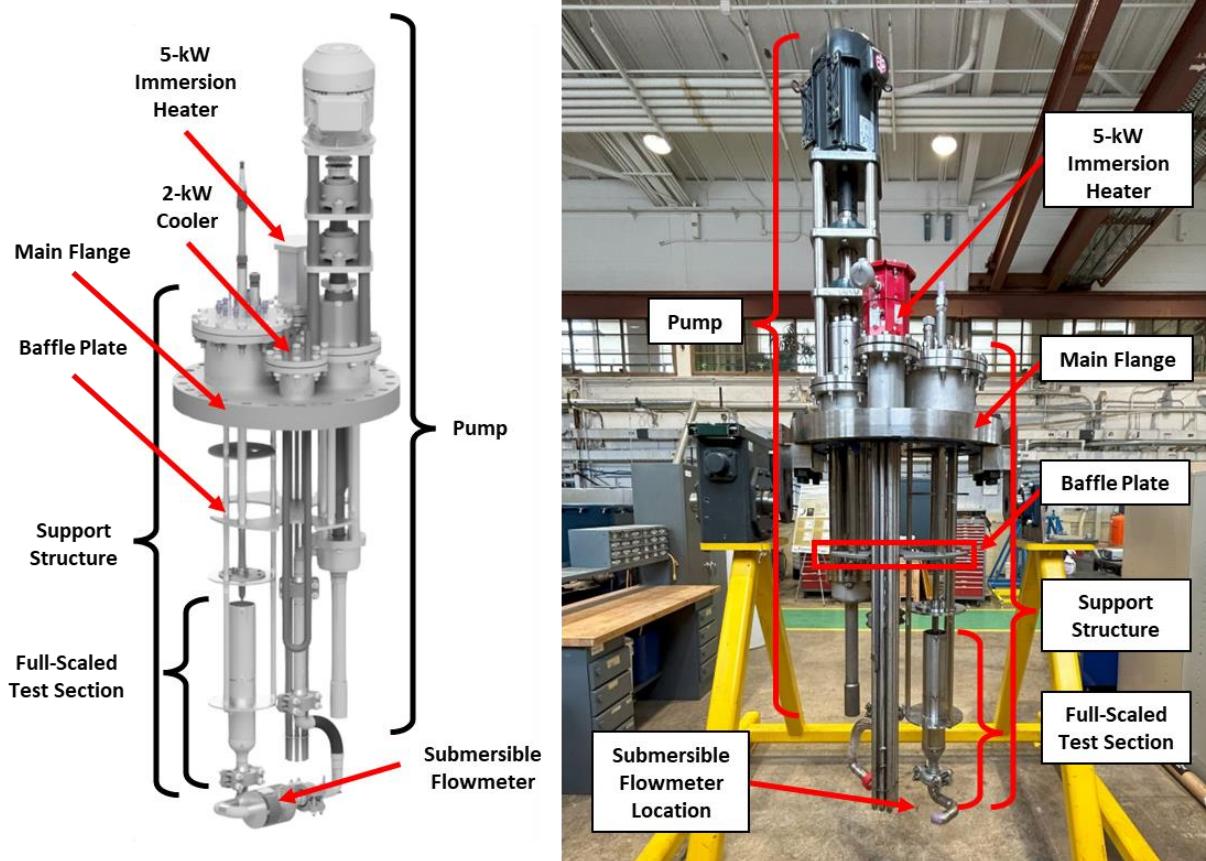


Figure 1 – A model view on the left and a photo of the F-STAr mock-up on the right. Note that the submersible flowmeter is not installed in the mock-up view.

For its first deployment, F-STAr will be setup to test liquid metal flow sensors, such as Eddy Current Flow Sensors based on the RDT C4-7T standard. To support testing these sensors, sub-test sections were designed and built to model Sodium Fast Reactor (SFR) outlet conditions. While F-STAr will initially be configured to test flow sensors, it can also be setup to meet a broad range of other experimental needs. Figure 2 shows three concept views of hypothetical F-STAr configurations. On the left is a fluidic diode, in the center is a temperature dependent orifice. And on the right is a heat exchanger. Other examples of configurations that F-STAr could support are hydrodynamic bearing testing, submerged electromagnetic pump testing, and thermal striping studies. In total, while it will be deployed to develop test flow sensors first, F-STAr is able to accommodate many experimental needs.

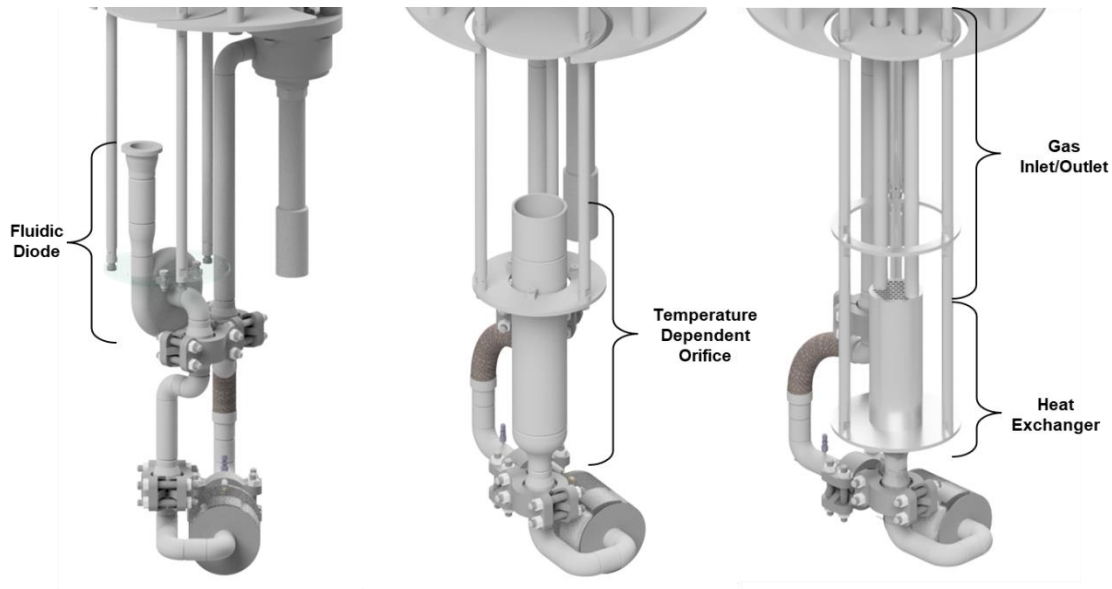


Figure 2 – Three concept views of hypothetical F-STAr configurations. Configurations shown are: a Fluidic Diode (left); a Temperature Dependent Orifice (center); and a heat exchanger (right).

This report will provide a status update on the assembly and initial qualification testing of F-STAr. All components have been manufactured and received. Some modifications to these components were made to support minor changes in the test article design. Additionally, the power distribution, and data acquisition and control enclosures were designed, completed, and tested along with the control system software. Furthermore, initial qualification testing was completed in water. Finally, the F-STAr submersible Electromagnetic Flowmeter (EMFM) was completed and calibrated in flowing sodium.

2 Introduction

A new generation of nuclear fission power plants are planning to use liquid metals as their primary system coolant. When compared to water, liquid metals have exceptionally good heat transfer characteristics and high boiling points, making them a highly effective coolant fluid. Specifically, at reactor operating temperatures the fluid properties of sodium are comparable to water. One such design aiming to leverage these unique properties is the Sodium Fast Reactor (SFR).

During SFR operations, monitoring flowrates through the individual fuel channels is essential and can be accomplished by installing flow sensors above the core. A class of sensors unique to liquid metals are ones based on Electromagnetic (EM) principles. In principle, these sensors produce a signal that is proportional to the fluid velocity as a liquid metal flowing through a magnetic field. In most cases, the fuel channel velocities in an SFR core are large. For example, a reactor with a 50,000 GPM core flowrate can have fuel channel velocities as high as 30 ft/s [1] [2] [3] [4] [5] [6] [7].

However, these large velocities present challenges for the development of liquid metal flow sensors. First, matching the high velocities requires large capacity pumps for testing. Additionally, some EM sensors may be sensitive to boundary conditions, requiring them to be calibrated in their exact deployment configuration. Unfortunately, in the United States experimental facilities that can meet these requirements are now nonexistent.

To address this testing capability gap, the Mechanism Engineering Test Loop (METL) is developing a new test article called the Flow Sensor Test Article (F-STAr). Figure 3 shows a Piping and Instrumentation Diagram (P&ID) of F-STAr as well as a model view with its primary components identified. Specifically, F-STAr includes a high-capacity pump rated to a nominal flowrate of 120 GPM; a support structure that can accommodate numerous experimental test sections; and lastly a heating and cooling system to control experimental conditions.

In this report, an update will be provided on the development of F-STAr, specifically on the assembly and water testing. Since the previous report, all F-STAr components have been manufactured and delivered. Moreover, the components were installed in an initial mock-up to check the fit and form of the test article. Figure 4 shows a photo of this mock-up in the B206 hi-bay without the submersible flowmeter installed. Additionally, the power distribution enclosure, control and data acquisition enclosures were designed, built, and tested along with the control system programming. Also, initial water testing of F-STAr was completed. Finally, the submersible flowmeter was completed and calibrated in flowing liquid sodium. The results of this calibration will also be discussed in detail.

3 Fabrication and Assembly

All F-STAr components have been manufactured, delivered, and inspected. Prior to water qualification, the test article was mocked-up in the B206 Hi-Bay to verify and check the fit and form. Figure 4 shows F-STAr after the mock-up was completed. First, the main flange was mounted to the 28-inch “A-Frame”. From there, individual sub-components were attached to the main flange. Additionally, the power distribution enclosure, data acquisition and control enclosure, and programming were designed, constructed, and qualified. Finally, the submersible flowmeter was also completed. In total, this section will summarize the initial mock-up of F-STAr and fabrication of the flowmeter.

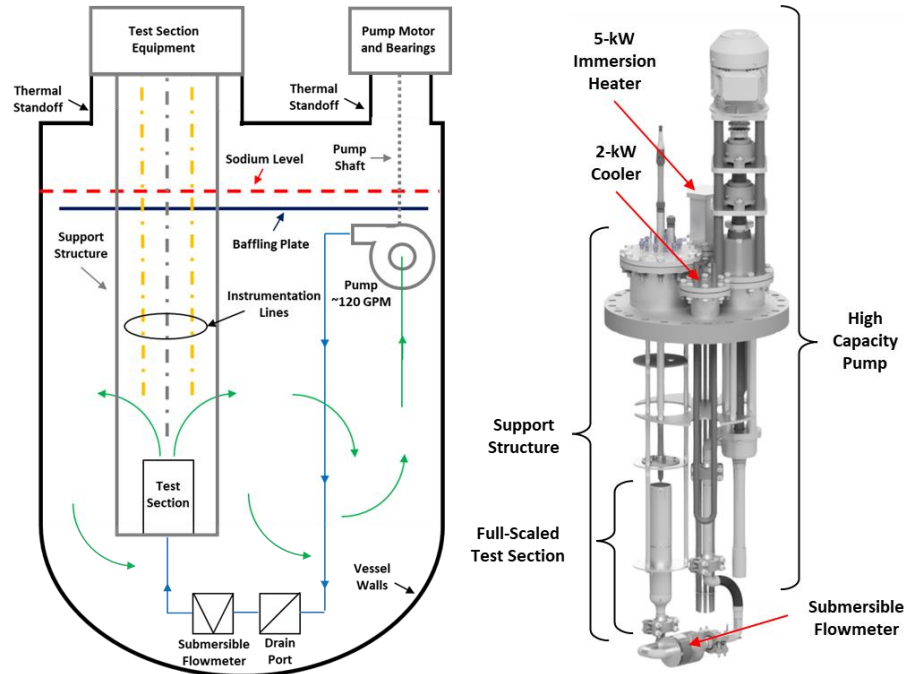


Figure 3 –A simplified P&ID diagram of F-STAr on the left. A model view of F-STAr annotated with the main components on the right.



Figure 4 – Mock-up of F-STAr prior to water testing in the B206 Hi-Bay. Note that the F-STAr Submersible EMFM is not installed.

3.1 Main Flange and Baffle Plate

F-STAr's central piece is the main flange. Figure 5 shows a top-down piece of the flange mounted to the 28-inch A-Frame. After mounting, the parallelness tolerance was estimated across each sub-flange. The pump, test section, and heater sub-flanges appeared to be within tolerance. However, the cooler sub-flange appeared to be out of tolerance by roughly 0.1-inches. This resulted in a noticeable lean in the cooler relative to the other components. However, for the initial application, this will be acceptable. Additionally, if a future application requires a tighter parallelism tolerance on the cooler sub-flange, there exists enough material to re-machine the top surface of the flange.

After mounting the main flange to the A-Frame and inspecting the sub-flanges, the baffle plating was installed. Figure 6 and Figure 7 show a top-down and bottom-up view of the baffle plate, respectively. This piece is intended to reduce churning at the free surface and to prevent splashing onto the bottom surface of the main flange. During installation, it was observed that with the tops of the struts installed flat to the main flange, the locational holes of the baffle plate did not line up. However, this issue was resolved by backing off the struts approximately 0.1-inches and using the free-play in the threading to align the holes.



Figure 5 – Top-down view of the F-STAr main flange mounted to the A-Frame flipper.



Figure 6 – Top-down view of the baffle plate used to reduce churning and splashing at the sodium surface.



Figure 7 – Bottom-up view of the baffle plate used to reduce churning and splashing at the sodium surface.

3.2 Pump

Next, the pump was installed onto the main flange. Figure 8 shows a photo of the pump installed onto the main flange with the baffle plating. Note that the volute was removed prior to installation so that the pump could fit through its sub-flange. The initial volute design was specified to have NPT connections. However, after an initial fit check with the inlet bell, it was determined that the threading would likely seize in a high temperature sodium environment. Therefore, the volute was modified to eliminate these connections and replace them with welds and Grayloc fittings. Figure 9 shows a photo of the modified volute, with the inlet bell welded directly to the bottom, and the outlet fitting changed to a Grayloc hub welded to an elbow. After these modifications were completed, the volute was mounted to the pump.



Figure 8 – F-STAR pump installed onto the main flange.



Figure 9 – Modified pump volute and inlet bell. Originally, the volute was designed to use NPT fittings. However, these were removed to avoid potential seizing during assembly and disassembly after sodium service.

3.3 Support Structure, UIS Baffle Plating, and Test Section

Prior to installation onto the main flange, the test section components were inspected. First, the test section flange was found to have normal instead of bored-through Swagelok fittings. Therefore, the flange was sent out for additional work to remove the inner lips of the fittings. Next, a locational hole in the Full-Scaled Test Section (FSTS) was found to be out of tolerance and an oblong shape. This was likely caused by either warping during welding, or the hole not being reamed during manufacturing. Instead of sending out the FSTS for additional work, it was noted that the other two holes would be enough to locate the support structure. Therefore, the oblong hole location was marked, and the bolt shoulder was machined down until it would pass freely through the hole.

After addressing the issues in the test section flange and FSTS, the test section stack-up was assembled on the test section assembly stand. Figure 10 shows a model view next to a photo of the completed stack-up with some important features annotated. The assembly proceeded smoothly, and all the components fit together well. Figure 11 shows a close-up photo of the FSTS with the Upper Internal Structure (UIS) baffle plating installed above, while Figure 12 shows a view looking down the FSTS and into the flow conditioner. Figure 13 shows a more detailed view of the UIS baffle plating. Note that the baffle plating is also used to position and locate the rabbit tube relative to the FSTS. Finally, Figure 14 shows the rabbit tube installed in its testing location. After assembly, longer rabbit tubes were ordered to allow for greater insertion length of the tube into the FSTS for flow sensor testing.

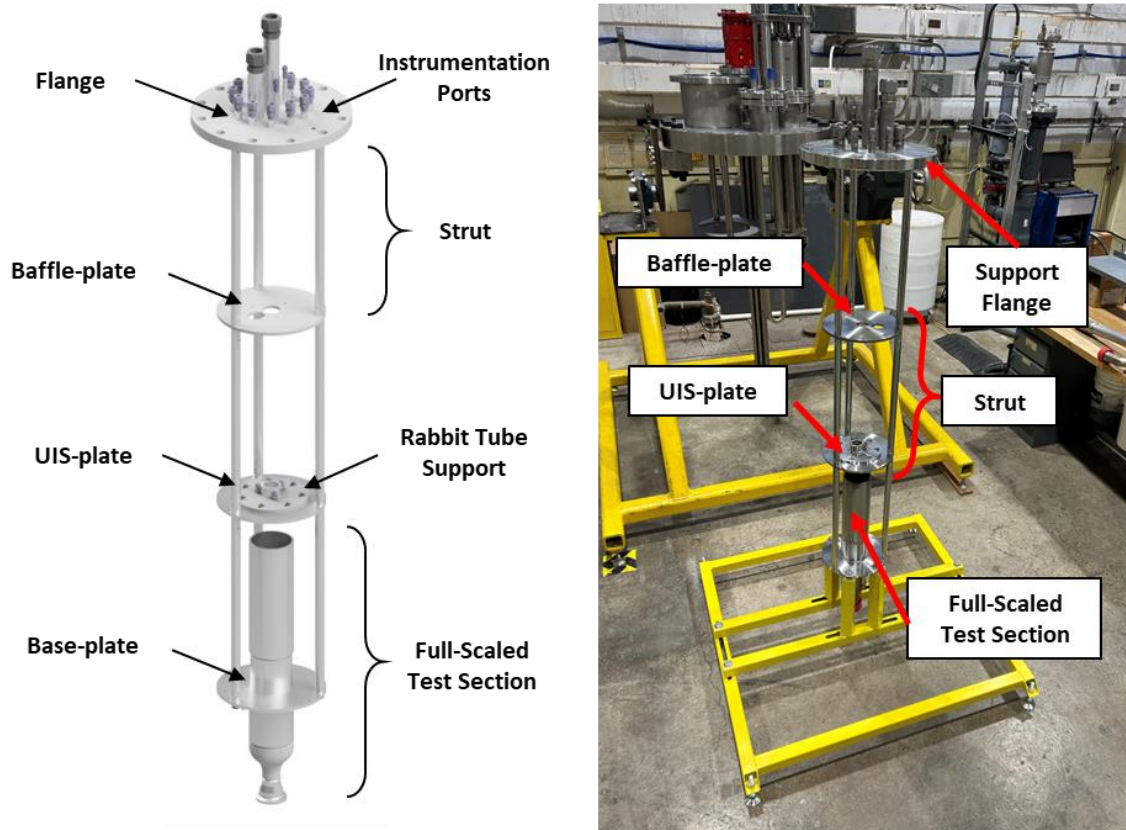


Figure 10 – Assembled Full-Scaled Test Section stack-up.

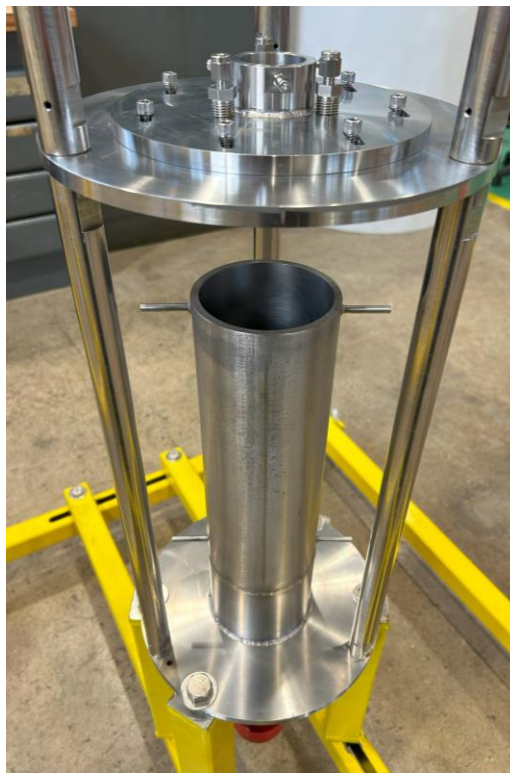


Figure 11 – Full-Scaled Test Section installed into the support structure stack-up.

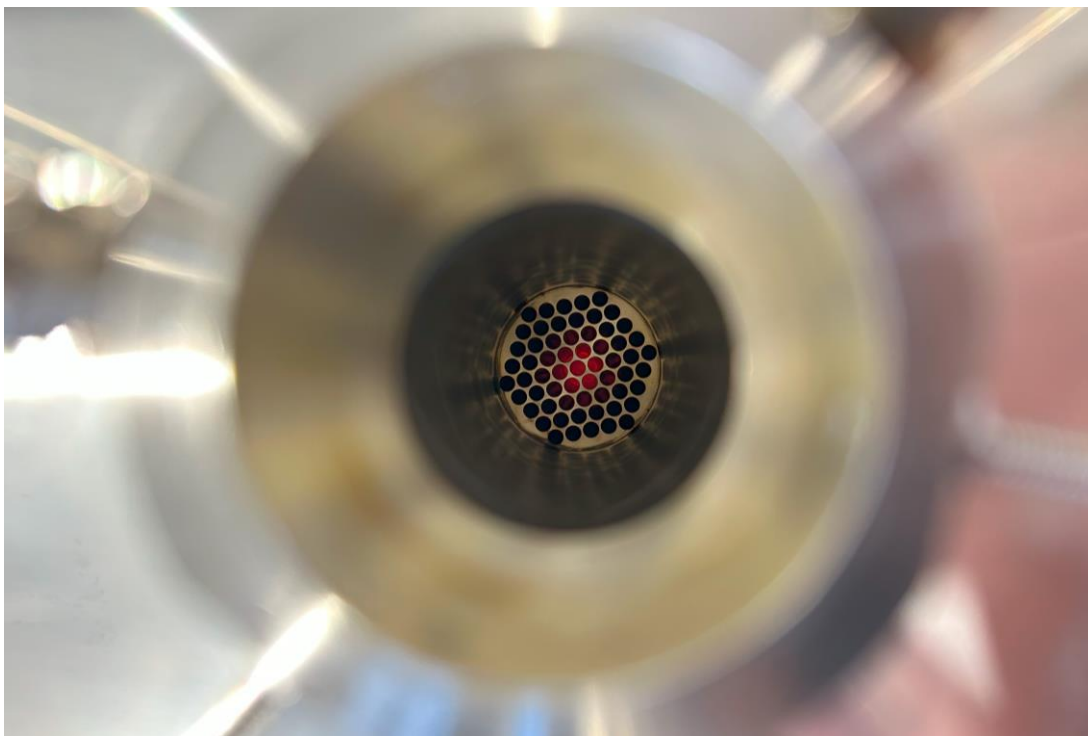


Figure 12 – View looking down the rabbit tube positioner and into the Full-Scaled Test Section flow conditioner.

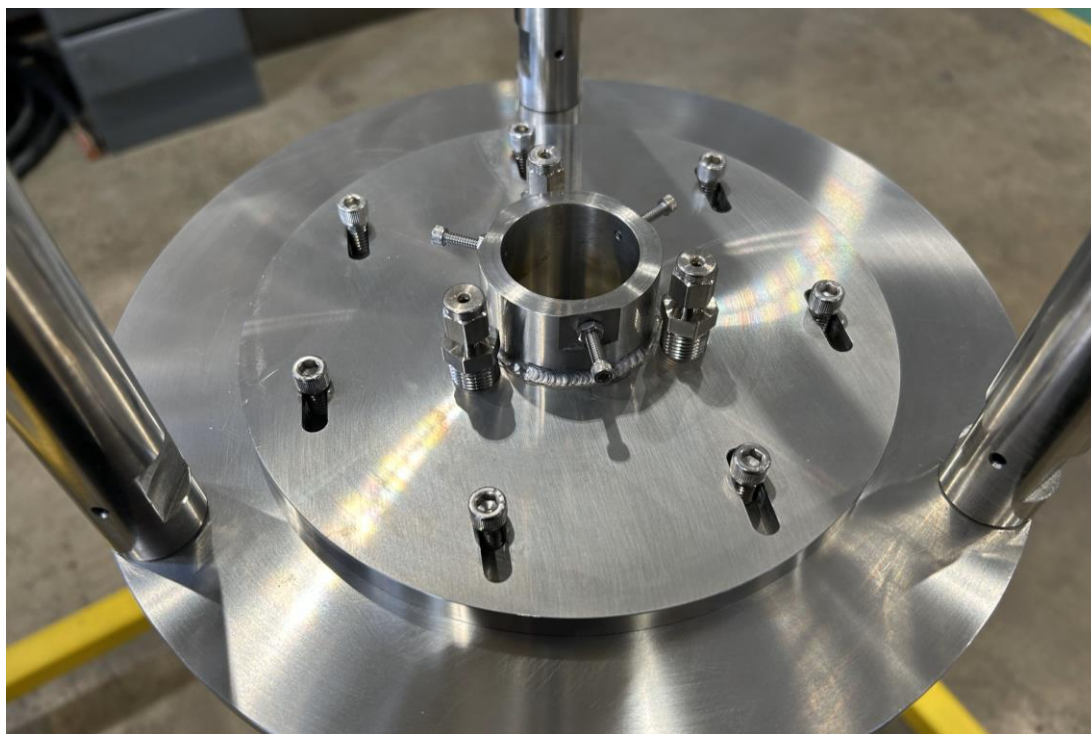


Figure 13 – Close-up view of test section baffle plate. This piece also doubles as a piece used to position the rabbit tube relative to the test section.



Figure 14 – Rabbit Tube positioned near Full-Scaled Test Section.

3.4 Heater and Cooler

As noted in the previous report [8], the heater was rejected and returned to the vendor to complete the required testing. This testing included a hydrostatic test, dye penetrant testing, as well as Mill Test Report (MTR) documentation. These tests were completed with the required documentation and the finished unit was received on 10/18/2022. Figure 15 shows the heater after it was removed from its shipping crate. After passing a receipt inspection, the heater was then installed onto the main flange and wired to its control unit. Additionally, the cooler was inspected and installed onto the main flange. Figure 16 shows a photo of the cooler prior to installation. Performance estimates of the cooler design can be found in earlier reports [9].

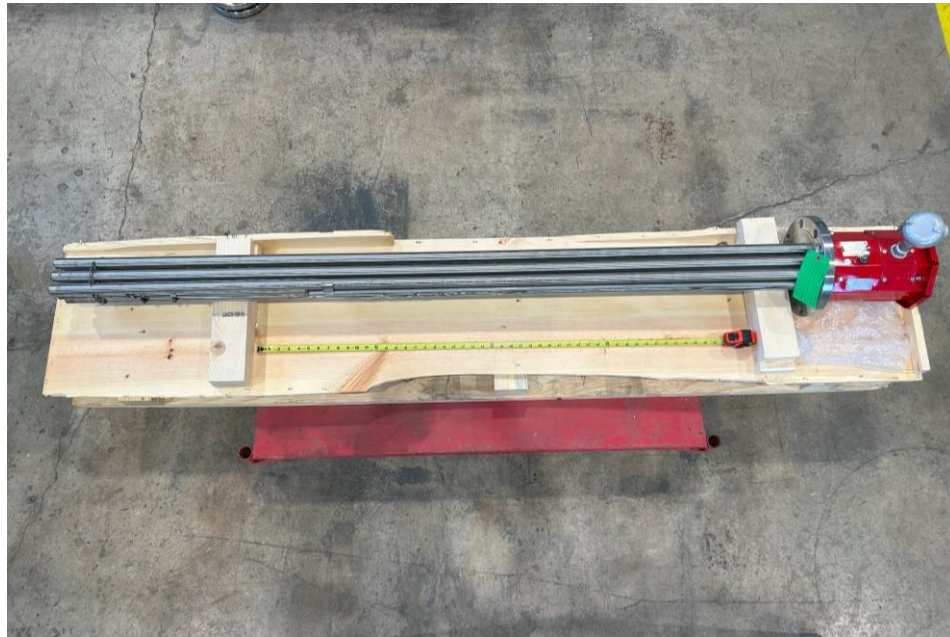


Figure 15 – Photo of immersion heater.



Figure 16 – Photo of the U-Tube immersion cooler.

3.5 Flowmeter

Since the previous report, the magnet-yoke was delivered, and the flowmeter was fabricated. Figure 17 shows a top-down view of the assembly that was delivered on 09/08/2022. A magnetic field measurement was made in the center of the magnet-yoke and compared to the results of the FEA analysis completed in an earlier report [8]. Figure 18 shows that that experimental measurement is within 5% of the FEA model, which was deemed sufficient for acceptance of the magnet-yoke assembly.

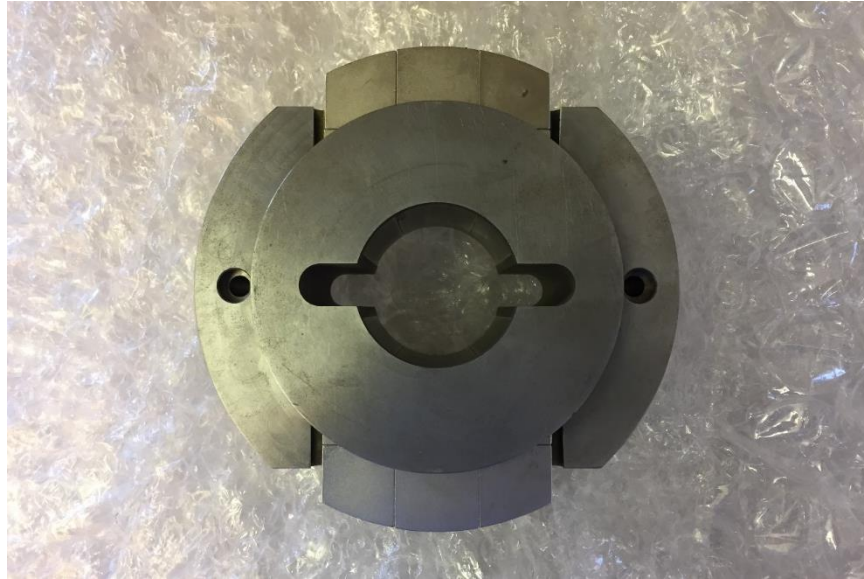


Figure 17 – Top-down view of the completed submersible EMFM magnet yoke.

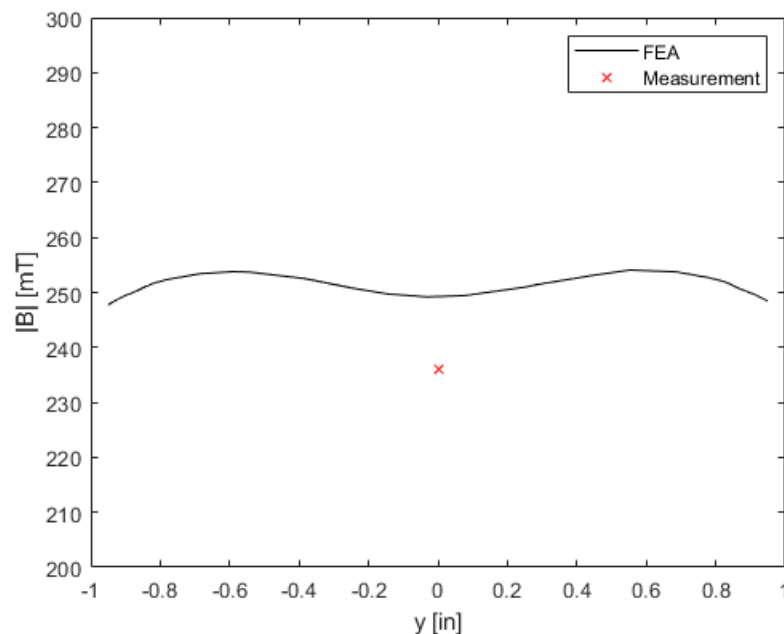


Figure 18 – FEA model of the centerline magnetic field as a function of magnet height plotted with a single experimental measurement.

After the magnet yoke assembly was received and accepted, construction of the F-STAr flowmeter resumed. Figure 19 shows a photo of the completed instrument. During construction, the primary contractor was unable to weld the transition pieces between the mineral insulated (MI) cabling and the flowmeter body. Therefore, a subcontractor was found that could successfully complete these joints. During discussions with this subcontractor, some design changes were made to the flowmeter to assist in completing the small transition piece welds. First, the signal and TC stand-offs were lengthened beyond the original length of the flowmeter to provide easier access to the backside of these joints. Secondly, an insert piece was added to extend the Grayloc fitting away from the stand-offs to allow the Grayloc clamp to be installed. Consequently, the extra length of the insert was taken from the flex-hose portion of the piping, which was shortened to accommodate the length of the insert.

Additionally, extra fittings were added to support the experimental calibration of the flowmeter. A 1.5-inch to 1-inch reducer and 1-inch Grayloc hub were welded to the opposite side of the 1.5-inch Grayloc hub. These fittings allow the flowmeter to interface with the sodium loop used during experimental calibration. More details on the calibration and experimental setup are described later in this report. After calibration, these fittings will be removed before the flowmeter is welded to the test section inlet.

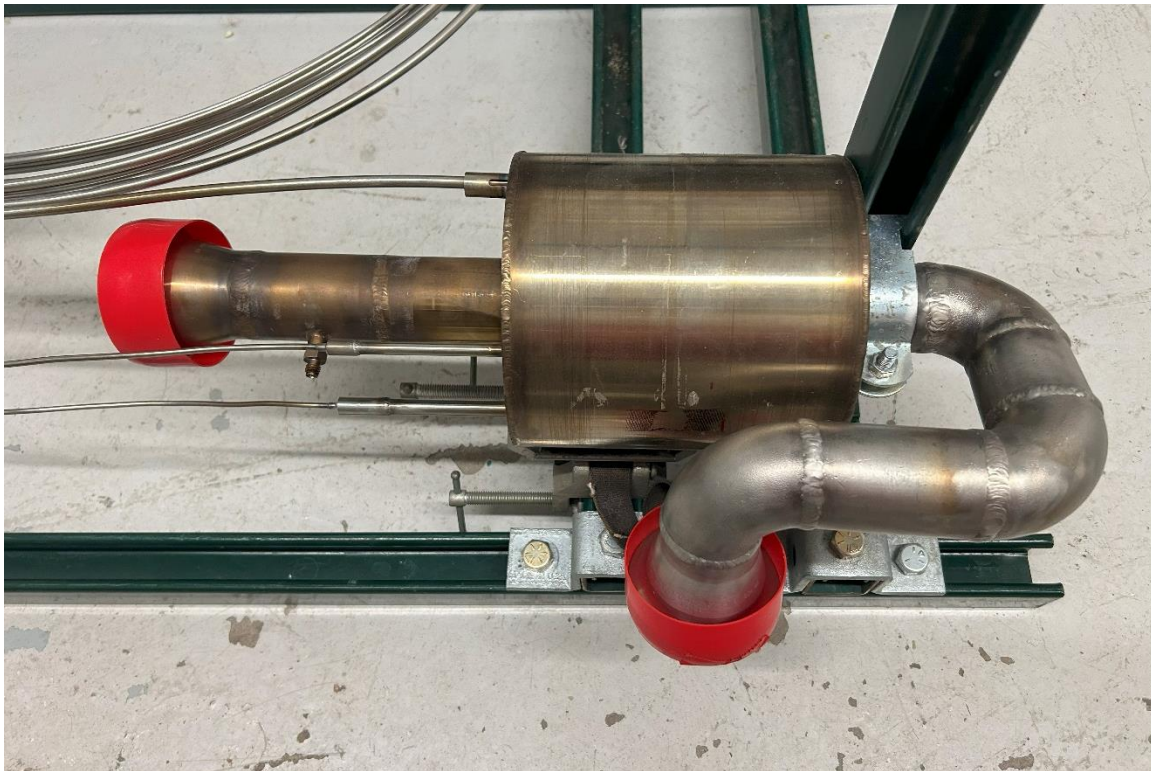


Figure 19 – Completed F-STAr submersible EMFM.

3.6 Power Distribution, Data and Control Systems

After the F-STAR mock-up was completed, several electrical enclosures were designed, built, and validated. These enclosures include the 480VAC Power Distribution (480-PD) enclosure and the Data Acquisition and Control (DAC) enclosure. Figure 20 shows these enclosures, along with the heater controller, mounted to a temporary frame. Note that the heater controller was designed and built by the heater manufacturer. The 480-PD enclosure distributes power to a Variable Frequency Drive (VFD) for the pump and a 24VDC power supply. A plug-and-cord supplies the 24VDC power to the DAC enclosure.

Inside the DAC enclosure is a National Instruments (NI) cRIO chassis used to read in thermocouple (TC) and analog signals, and to send digital and analog signals. Additionally, the DAC enclosure includes an Emergency Stop (E-Stop) system for the pump and heater that is hard wired to mechanical relays. Communicating with the cRIO is a virtual interface programmed using NI's LabVIEW.

Both the 480-PD and DAC Enclosure were tested prior to connecting F-STAR components. Additionally, the programming was tested and validated to ensure the analog signals were read in properly, the analog and digital outputs were correct, and that the E-Stop system functioned as intended. After successful validation test of these systems, F-STAR components such as the pump and heater were connected to power to perform preliminary water validation tests.



Figure 20 – 480 VAC Power Distribution (left), Data Acquisition and Control (center), and Heater Controller (right) enclosures setup on a temporary frame.

4 Initial Water Testing

Before insertion into METL's sodium system, F-STAr's operation and performance were qualified in water. The purpose of the qualification tests was to verify the performance of the pump and to observe the behavior of the test article in a flowing fluid environment. Note that this water testing did not aim to achieve dimensional similitude with sodium. For these qualification tests, the fluid properties of water at room temperature and pressure were close enough to sodium to provide an estimate of the performance and behavior. The water qualification testing provided measurements and observations of the pump's performance, estimates of the system loss curves, flow patterns near the fluid free surface, and vibrations of F-STAr's components. To accomplish this, F-STAr was inserted into a large plastic tank and filled with de-ionized (DI) water. This section of the report describes the results of the preliminary water qualification testing.

4.1 Water System and Setup

A Water Fill and Purification system was set up to support the water qualification testing. Figure 21 shows a photo of the water system, which includes a 260-gal water testing tank in the back-left, a 1000-gal DI water storage tank with purification system in the back-right, and a fill system in the front-center. DI water was used to prevent mineral build-ups on the tested components. The water in the storage tank was periodically circulated through the purification system strainer to filter out larger particulate matter and through an ultra-violet light (UV) system to remove any biological buildup such as algae. After water purification, the valve lineup can be switched to fill the water testing tank from the storage tank. Conversely, the valve lineup can be switched to drain the water testing tank to the storage tank. For water qualification runs, F-STAr was lifted off the A-Frame and the water testing tank placed below. Then, F-STAr was lowered into the tank and reinstalled on the A-Frame.



Figure 21 – Water Fill and Purification system used to fill the water testing tank on the left.

Flow Sensor Test Article (F-STAr) – Assembly and Water Testing Report

August 2023

F-STAr's reference flowmeter was specifically designed to work in sodium. Therefore, a different setup was created to measure flowrates for water qualification testing. Figure 22 shows a photo of the initial water setup. Flowrates were measured using a 1.5-inch nominal diameter, Blancett turbine flowmeter. To obtain the best possible results with this flowmeter, the piping sections were sized to allow an appropriate entrance and exit length as recommended by the manufacturer. Additionally, a pair of pressure taps were installed to measure the differential pressure across the pump. These taps were installed in the pump inlet bell and in a port just downstream from the flexible bellows hose.

Note that this setup is considerably different than the sodium setup. First, the turbine flowmeter has higher pressure losses than the F-STAr flowmeter. Additionally, more plumbing was used in this setup than the sodium setup. Secondly, the high-pressure tap is located downstream from the flexible bellows hose, which itself has higher pressure losses. Consequently, the pressure-flowrate results from this testing are assumed to be a conservative approximation to the actual curves. This is due in part to the higher system losses caused by the turbine flowmeter and extra plumbing. And due to the placement of the high pressure tap downstream from the flexible bellows hose.

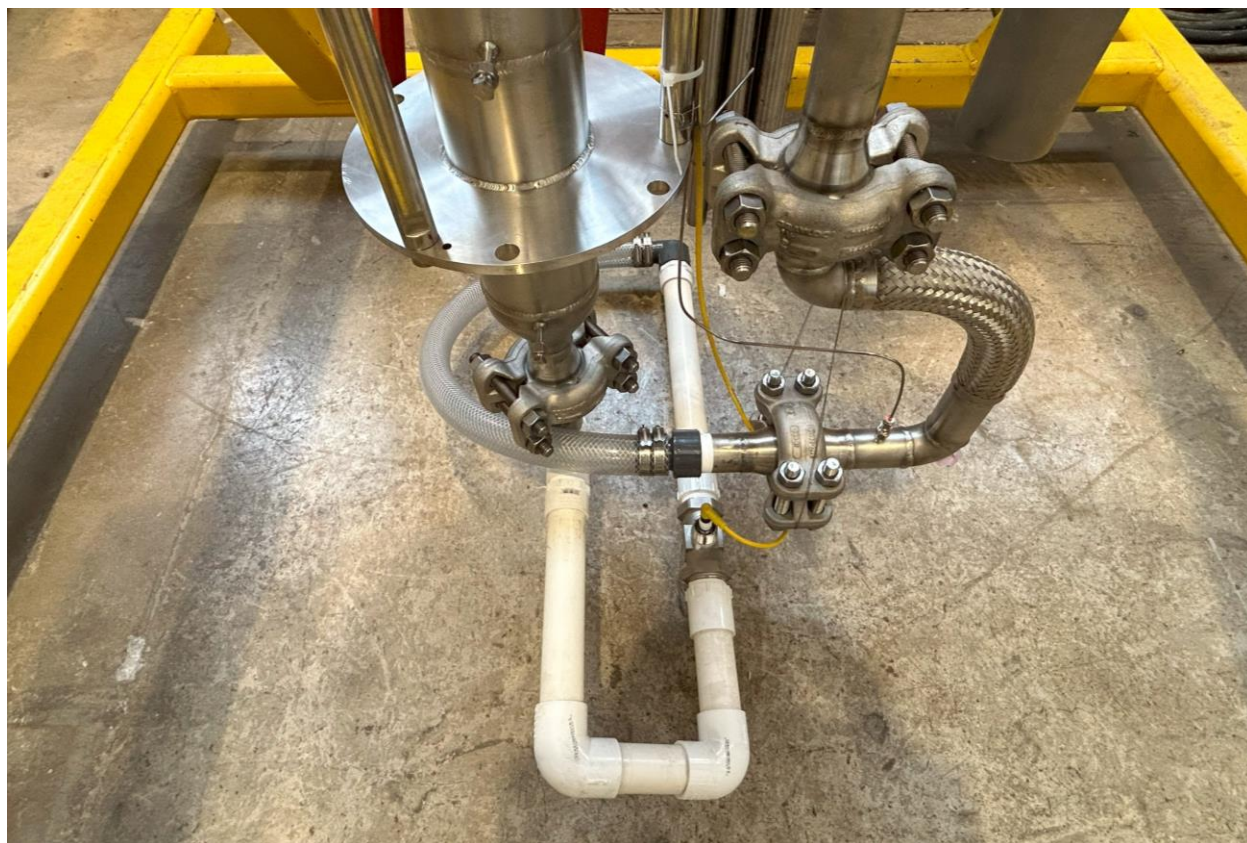


Figure 22 – Setup used for water qualification testing of F-STAr. Note that this setup uses a turbine water flowmeter and significantly more piping than the sodium setup, meaning that pressure losses in this configuration were assumed to be higher than those in the sodium configuration.

4.2 Water Testing and System Loss Curves

Pressure-flowrate curves in the water qualification setup were created by gradually stepping up the pump speed and measuring the corresponding pressure and flowrate. Figure 23 presents the initial water testing results in dark blue “X’s”. The dark blue dashed line is an extrapolation of experimental data using a quadratic polynomial fitted using a linear least squares approach. Note that the dark blue curve shows the pressure losses as a function of flowrate for the water system. In this case, the pressure losses of the water system will be larger than those of the sodium system at a given flowrate.

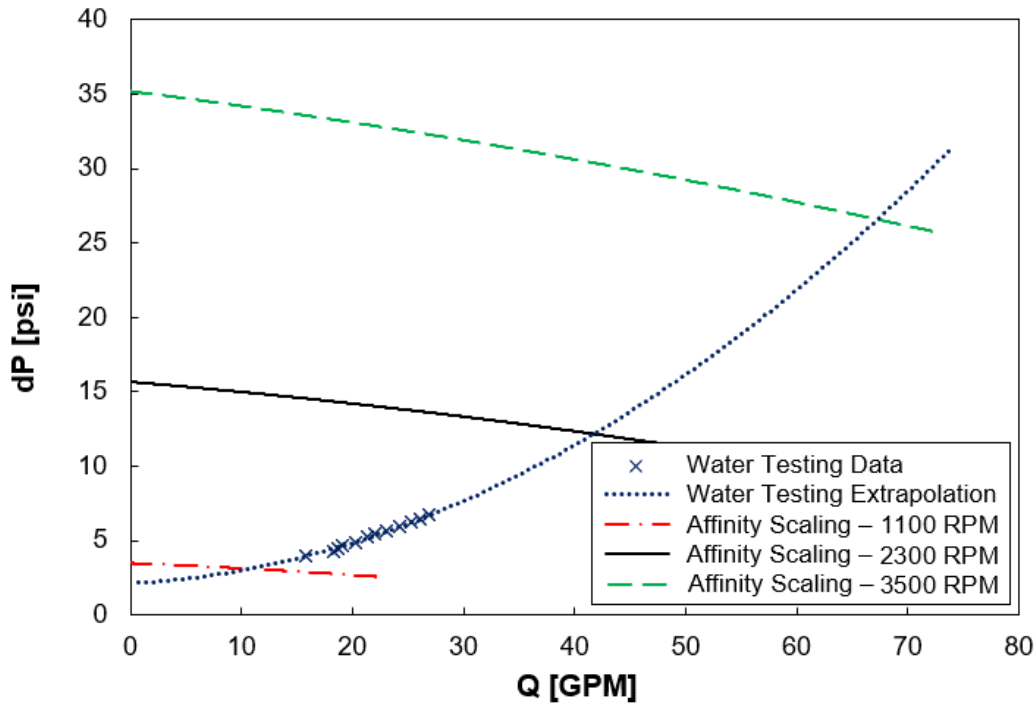


Figure 23 - F-STAr system loss curves plotted with estimated pump curves derived from THETA's pump using affinity laws.

Also plotted are three pump curves. Note that these curves were derived from THETA pump data [10] using pump affinity laws. Equation 1 shows the affinity law used to scale the data, which states that the ratio of flowrates Q is proportional to the ratio of the pump impeller diameters. In this case, F-STAr's flowrate and impeller diameter are Q_2 and D_2 , respectively, while THETA's flowrate and impeller diameter are Q_1 and D_1 , respectively. This method was assumed to provide a good estimate since both F-STAr's and THETA's pumps are similar. Future work includes measuring actual pump curves for F-STAr's pump versus using scaled data. Additionally, it is important to note that the lowest rated flowrate the turbine flowmeter can measure is 15-GPM. Furthermore, the highest flowrate measured was limited due to excessive vibrations in the pump.

$$Q_2 = \frac{D_2}{D_1} \cdot Q_1$$

Equation 1

Figure 23 estimates that the F-STAr pump will achieve a maximum flowrate of approximately 67-GPM. This is significantly lower than the desired 120-GPM first reported during factory testing [8]. As noted earlier, it is likely that the flowrate performance is lower due to higher pressure losses in the water qualification setup compared to the factory water tests. Therefore, future work includes setting up a simplified water qualification system to measure the actual pump performance curves. Additionally, future work includes investigating methods to improve the pump's performance to achieve higher flowrates.

Also observed during water qualification testing were excessive vibrations at high rotational speeds. Above 1825-RPM, the pump was observed to vibrate aggressively and shake the assembly. Multiple speed values were tried to determine if the observed vibrations were contained in resonance modes or if they were constant. Initial tests up to 75% full speed show a significant constant vibration versus discrete resonant modes. The vibrations were significant enough to shake objects tens of feet away from the A-Frame. Future work includes troubleshooting the pump to reduce the magnitude of the vibrations so that the full performance of the pump can be accessed.

5 Flowmeter Calibration

F-STAr's submersible Electromagnetic Flowmeter (EMFM) was calibrated in liquid sodium prior to installation. This work was completed at an outside contractor's sodium loop using a NIST traceable reference flowmeter over a volumetric flow range of 3.5-GPM to 18-GPM at 200-C and 400-C. The purpose of this testing was to verify the functionality, wet the conduit walls, verify the temperature compensation methods, and to provide an experimental calibration over a partial range of the EMFM. Ideally, the EMFM would have been calibrated over the full range, from 0.5-GPM to 120-GPM or higher. However, a calibration flow loop of this size is not currently available. Future work with the EMFM includes building a multi-physics model validated against the experimental data, and then using this model to provide an extrapolated calibration curve. This section of the report describes the calibration methodology, discusses the uncertainty analysis, reviews the experimental setup, and provides the final calibration curves.

5.1 Methodology

The F-STAr submersible EMFM was calibrated directly against a 1-inch nominal diameter, Foxboro M83F vortex shedding flowmeter. Figure 24 shows a model of the calibration setup with the vortex shedder located just upstream from the F-STAr reference flowmeter. During the calibration, volumetric flowrates were varied from 4-GPM to 18-GPM over 1-GPM increments at 200-C and 400-C. The vortex shedder reading, and F-STAr reference flowmeter signal were measured over a 90-second interval at each increment.

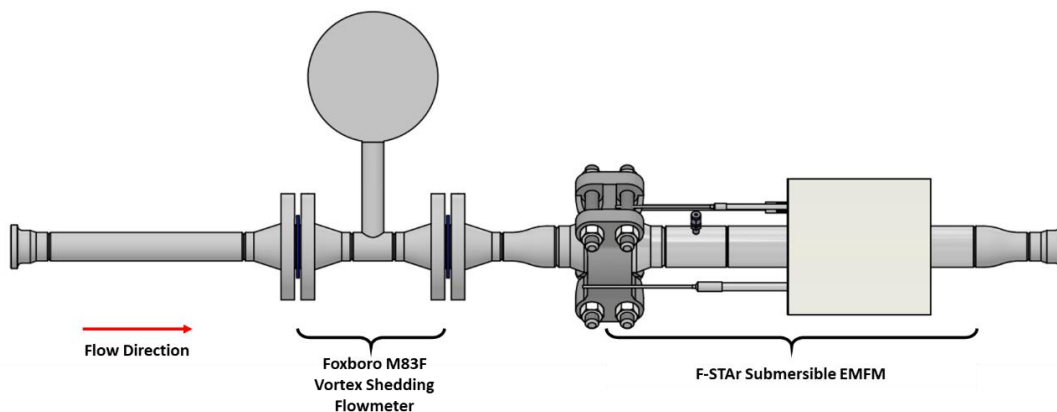


Figure 24 – F-STAr submersible EMFM calibration setup model.

A calibration coefficient was defined to correct the EMFM flowrate measurements. Equation 2 defines the calibration coefficient as the ratio of the vortex shedder mass flowrate, \dot{m}_{ref} , and the F-STAr EMFM mass flowrate, \dot{m}_{EMFM} .

$$C = \frac{\dot{m}_{\text{ref}}}{\dot{m}_{\text{EMFM}}}$$

Equation 2

Equation 3 derives the vortex shedder mass flowrate as the measured volumetric flowrate, Q_{ref} , multiplied by the temperature dependent sodium mass density, $\rho(T_{\text{Na}})$.

$$\dot{m}_{\text{ref}} = \rho(T_{\text{Na}}) \cdot Q_{\text{ref}}$$

Equation 3

Equation 4 defines the F-STAr EMFM mass flowrate, where d_i and D_o are the inner diameter and outer diameter, respectively, L is the length, V_{EMFM} is the measured signal, b_0 is the effective magnetic field magnitude, T_m is the magnet temperature, K_1 is the wall-shunting correction factor [11] [12] [13], K_2 is the end-shunting factor [14] [15] [16] [17], and K_3 is the magnet temperature correction factor [18] [19].

$$\dot{m}_{\text{EMFM}} = \frac{\rho(T_{\text{Na}}) \cdot \frac{\pi}{4} d_i \cdot V_{\text{EMFM}}}{b_0 \cdot K_1(T_{\text{Na}}, D_o, d_i) \cdot K_2(L, d_i) \cdot K_3(T_m)}$$

Equation 4

Equation 5 shows the simplified version of the calibration coefficient C , derived by substituting Equation 3 and Equation 4 into Equation 2.

$$C = Q_{\text{ref}} \cdot \frac{b_0 \cdot K_1(T_{\text{Na}}, D_o, d_i) \cdot K_2(L, d_i) \cdot K_3(T_m)}{\frac{\pi}{4} d_i \cdot V_{\text{EMFM}}}$$

Equation 5

5.2 Uncertainty Analysis

5.2.1 Uncertainty Budget

An uncertainty analysis of the F-STAr EMFM was completed to estimate the accuracy of the flow measurements. First, the uncertainties of the variables in Equation 5 were budgeted. Table 1 summarizes the estimated bias and precision errors, $U_{b,j}$ and $U_{s,j}$, respectively.

Table 1 – Budget of estimated uncertainties of the measured variables during calibration of the F-STAr reference flowmeter.

Variable	Source	$U_{s,i}$	$U_{b,i}$
T_{Na}, T_m	Thermocouple	-	$\pm 1^\circ\text{C}$
	NI 9213	-	$\pm 1^\circ\text{C}$
B_0	Gauss Meter	-	$\pm 0.1\text{ mT}$
D_o, d_i	Micrometer	-	$\pm 0.0005\text{ in}$
L	Calipers	-	$\pm 0.001\text{ in}$
V_{EMFM}	NI 9219	$\pm 0.1\%$	$\pm 0.08\text{ mV}$

As specified by the manufacturer, the vortex shedder accuracy is Reynolds number dependent. Table 2 shows accuracy as a function of Reynolds number and shows the corresponding volumetric flowrate calculated in sodium at 200-C and 400-C. Note that the sodium properties were obtained from Fink [20].

Table 2 – Accuracy of the vortex shedding flowmeter. The flowrates were calculated using a 1.63-inch inner diameter with sodium properties evaluated using Fink.

Reynolds Number	200-C Flowrate [GPM]	400-C Flowrate [GPM]	Accuracy [%]
20,000-30,000	5.5-8.2	3.5-5.2	1
30,000-200,000	8.2-54.7	5.2-34.6	0.5
>200,000	>54.7	>34.6	1

5.2.2 EMFM Calibration Uncertainty

The F-STAr EMFM uncertainty was estimated following the methods described in the ISO Guide to the Expression of Uncertainty in Measurement [21]. As described in the ISO Guide, there are two types of uncertainties to consider. First are Type A uncertainties, which are assigned to the random fluctuations of the readings observed during measurement. Equation 6 accounts for these uncertainties where N is the number of measurements, C_i is the calibration coefficient calculated at the i^{th} measurement, and \bar{C} is the average of the calibration coefficient over all N measurements.

$$U_{c,\sigma} = \frac{\sigma}{\sqrt{N}} = \sqrt{\frac{1}{N(N-1)} \sum_{i=1}^N (C_i - \bar{C})^2}$$

Equation 6

The second type of uncertainties are Type B, which are assigned to the measurement errors of the constitutive variables of the calibration coefficient. These uncertainties include bias errors B_R and precision errors S_R that are propagated through Equation 5 using the general law of propagation. Equation 7 defines the bias error and Equation 8 defines the precision error where $U_{b,j}$ and $U_{s,j}$ are the bias and precision errors, respectively, defined in Table 1 and Table 2. Equation 9 defines the partial derivative of the calibration coefficient to the j^{th} constitutive variable of the calibration coefficient. Finally, Equation 10 estimates the total calibration coefficient as the quadrature sum of all Type A and Type B uncertainties where t_{α,ν_R} is the corresponding t-distribution for the specified confidence interval and degrees of freedom.

$$B_R = \sqrt{\sum_{j=1}^{N_B} (\theta_j U_{b,j})^2}$$

Equation 7

$$S_R = \sqrt{\sum_{j=1}^{N_s} \left(\theta_j \frac{x_j \cdot U_{s,j}}{\sqrt{N}} \right)^2 + U_{c,\sigma}^2}$$

Equation 8

$$\theta_j = \frac{\partial C}{\partial x_j}$$

Equation 9

$$U_C = \sqrt{B_R^2 + t_{\alpha, \nu_R} S_R^2}$$

Equation 10

5.3 Experimental Setup

Calibration of the F-STAr EMFM was completed at an outside contractor's sodium facility. Figure 25 shows the actual setup that was sketched out in Figure 24. Prior to installation, each section was instrumented with thermocouples and trace-heated flexible heat tapes. Then, the entire section was insulated. To support the test section in the sodium loop, the assembly was floated using a pair of springs. Before pre-heating the assembly, a vacuum was pulled on the EMFM snorkel tube to evacuate it. Then, the volume was backfilled with 5-psig of Argon gas to provide an inert environment to prevent oxidation of the magnet coating in air at high temperatures. After the assembly was preheated, the system was filled with sodium at 200-C, and flow was initiated. Once a signal was obtained from the F-STAr EMFM, conduit wall wetting and calibration runs were started.

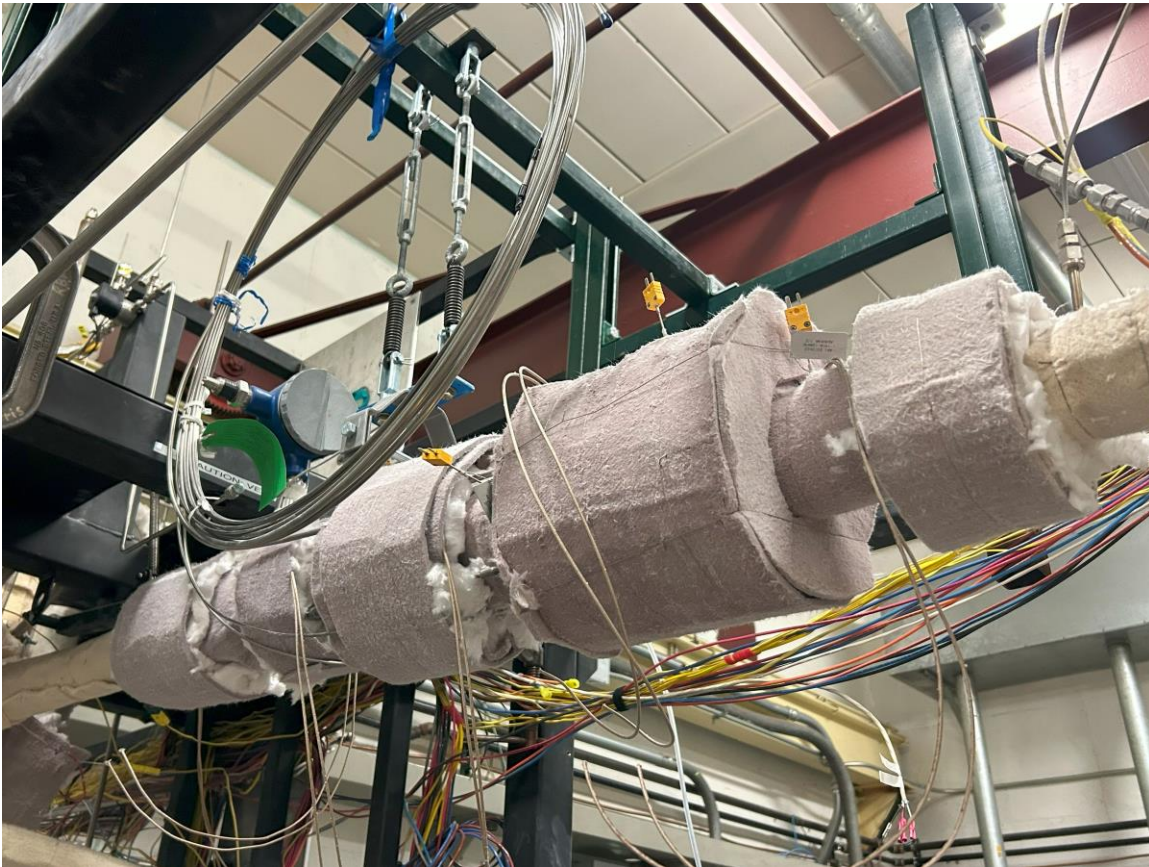


Figure 25 – Experimental setup for sodium calibration of the F-STAr EMFM.

5.4 Calibration

5.4.1 Conduit Wall Wetting

Prior to calibrating the F-STAr EMFM, the conduit walls were wetted to ensure good contact between the sodium, inner conduit wall, and external measurement leads. Experience with sodium has shown that it has poor initial surface wetting characteristics [22]. This will impact the electrical resistance between the sodium and the measurement leads, which will therefore impact the measured signal. However, as the walls are exposed to sodium, the surface composition will change, with the wettability of the surface enhanced. This phenomenon is temperature dependent and can be accelerated at higher temperatures. Therefore, prior to calibration, a constant 6.5-GPM flowrate of 400-C sodium was passed through the EMFM, and the signal was measured over time. Once the signal reached an asymptotic steady state, the conduit walls were assumed to be wetted.

Figure 26 shows the normalized EMFM signal as a function of time. Equation 11 shows that the normalized signal Δ_{EMFM} is simply the difference between the EMFM flowrate and the reference flowrate, normalized by the reference flowrate. Additionally, Figure 26 shows the pump speed, sodium temperature, magnet temperature are plotted over time as well. Note that the normalized signal and pump speed values are both referenced on the left axis. One can see that an initial wetting phase occurred during the first two hours of testing, after which the flowmeter signal reached an asymptotic value.

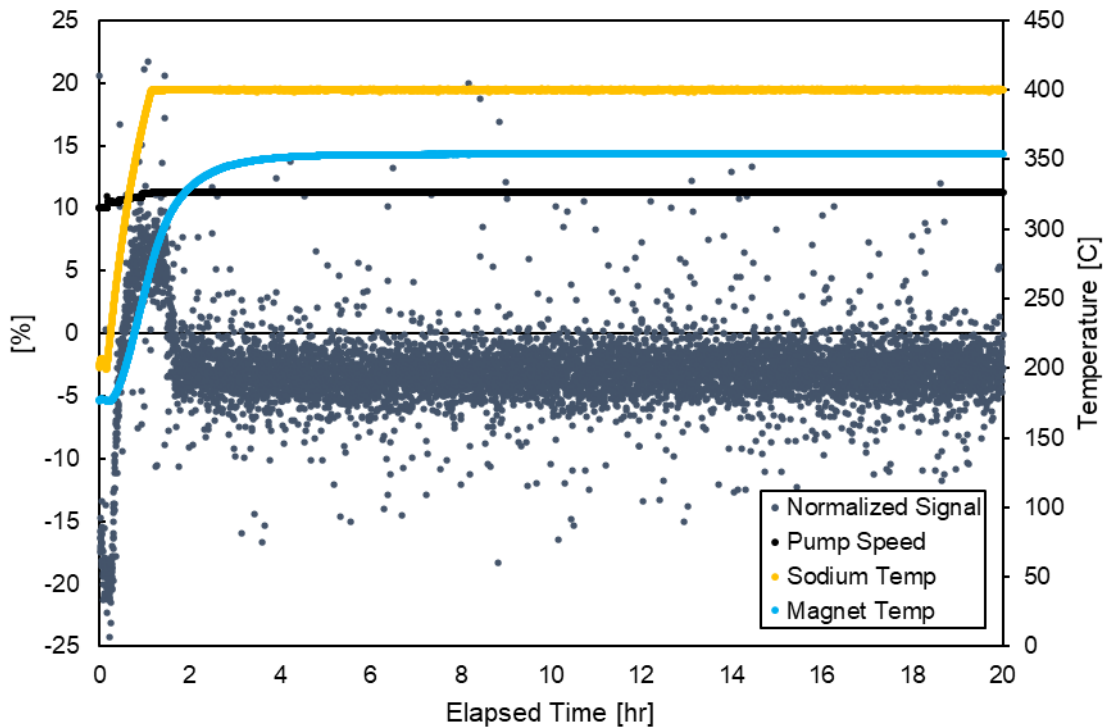


Figure 26 – Normalized EMFM signal, pump speed, sodium temperature, and magnet temperature over an elapsed time of 20-hrs. Note that the normalized signal and pump speed are both referenced on the left axis. After an initial wetting phase over the first two hours of testing, the EMFM signal reached an asymptotic value.

$$\Delta_{EMFM} = \frac{Q_{EMFM} - Q_{ref}}{Q_{ref}} \cdot 100 [\%]$$

Equation 11

5.4.2 Calibration Curves

After the wetting of the flowmeter conduit walls was completed, the calibration testing began. The calibration data obtained by varying the volumetric flowrate from 4-GPM to 18-GPM over 1-GPM increments at 200-C and 400-C. For data analysis, it is more concise to convert the volumetric flowrates to mass flowrates. Therefore, Figure 27 presents the calibration data, with the range of mass flowrates covering 0.16-kg/s and 0.94-kg/s. Figure 28 plots the average calibration coefficient defined in Equation 5 with error bars as function of the average mass flowrate. Note that \tilde{C} appears to have some dependency on the mass flowrate of sodium. This phenomenon was observed in other flowmeters of this type and is thought to be caused by the induced currents being carried downstream, reducing the signal measured at the lead contact points [19].

Therefore, Equation 12 was used as a model the calibration coefficient \tilde{C} as a function of the calculated mass flowrate. Table 3 presents the coefficients and standard errors of Equation 12 derived from a linear regression analysis. Note that the regression analysis was applied to the transformed version of Equation 12, shown in Equation 13. Finally, Equation 14 presents the calibrated EMFM mass flowrate, where \tilde{C} is the fitted calibration coefficient as a function of \dot{m}_{EMFM} defined in Equation 12, and \dot{m}_{EMFM} is the uncorrected EMFM mass flowrate defined in Equation 4.

Due to the limited testing capabilities currently available, the flowmeter could not be calibrated over the entire range of flowrates. Therefore, until a facility becomes available for direct calibration, the flowmeter will be relying on extrapolations from the calibration data. However, since the method described results in a non-linear calibration, extrapolating Equation 12 will be limited. Thus, a numerical model of the F-STAr flowmeter will be developed following the previously completed work on THETA's flowmeter [19]. The model outputs will be compared to the recorded experimental data for validation. Then, the model will be used to extrapolate the calibration to the intended maximum flowrate.

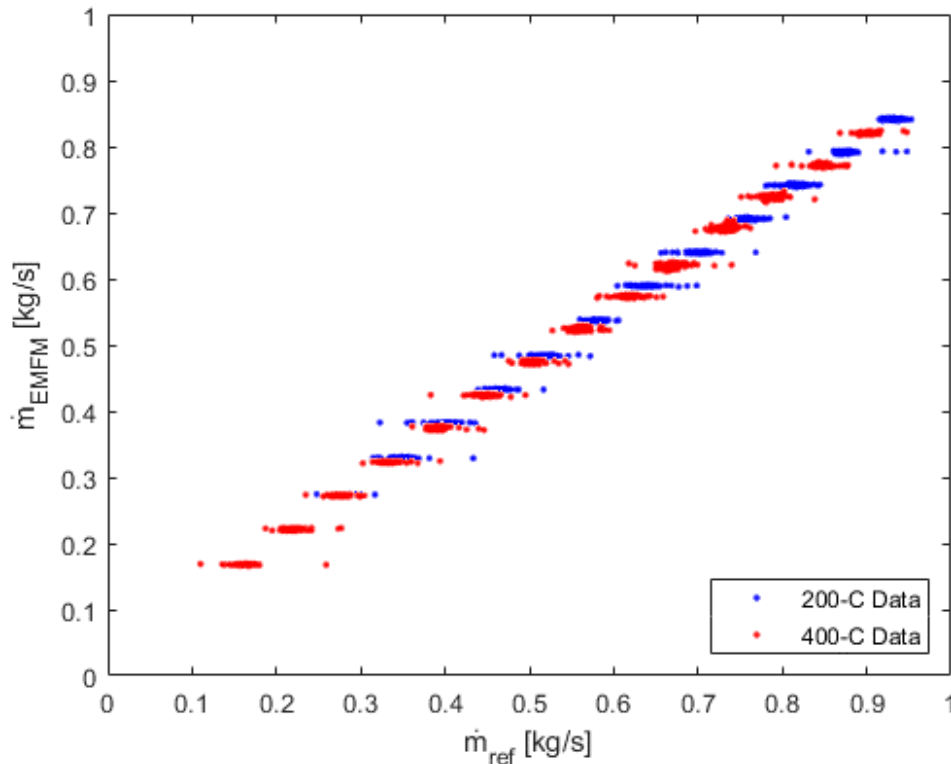


Figure 27 – Flowmeter calibration curves at 200-C and 400-C.

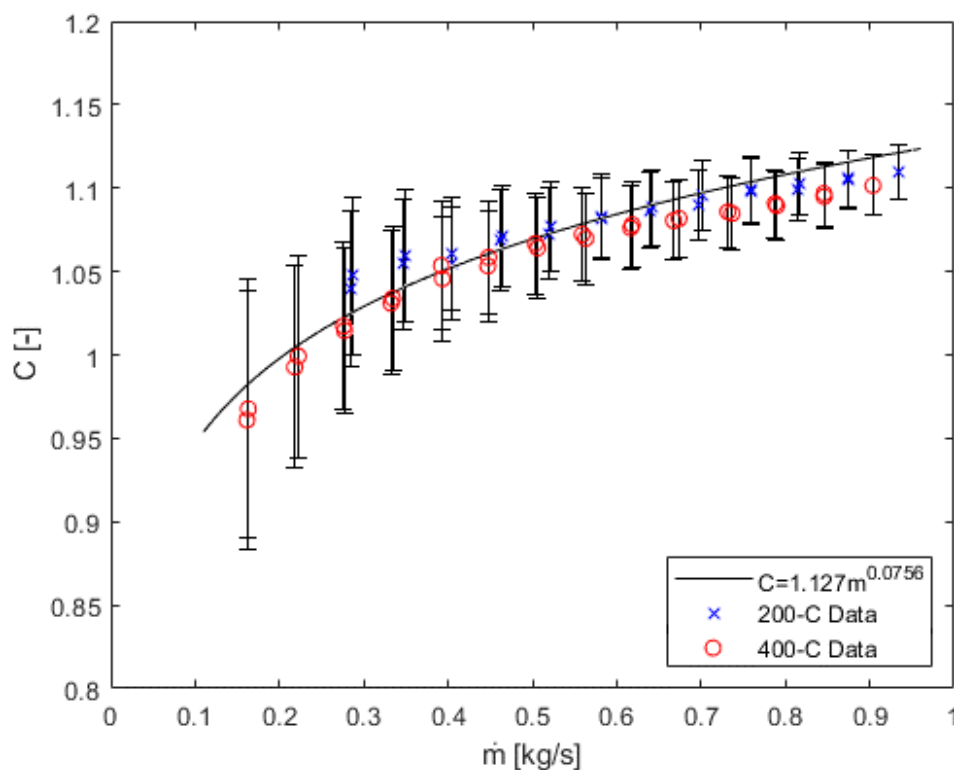


Figure 28 – Calibration coefficient calculated using Equation 5 with error bars.

$$\tilde{C} = \alpha_0 \cdot \dot{m}_{EMFM}^{\beta_0}$$

Equation 12

Table 3 – Coefficients and standard errors of Equation 12.

	$\alpha_0 [s/kg]$	$\beta_0 [-]$
Coefficient	1.127	0.0756
Standard Error	1.001	0.0009

$$\log_{10}(\tilde{C}) = \beta_0 \log_{10}(\dot{m}_{EMFM}) + \log_{10}(10^{\alpha_0})$$

Equation 13

$$\dot{m} = \tilde{C} \cdot \dot{m}_{EMFM}$$

Equation 14

5.4.3 Error Estimate

Next, the total uncertainty of the F-STAr EMFM was estimated. First, the total error was estimated to be the analytically calculated total calibration coefficient error, U_C , normalized by C . Second, Equation 15 was used to calculate the normalized difference between the calibrated EMFM flowrate and reference flowrate. Figure 29 plots both error estimates at 400-C and 200-C. One can see that the analytically calculated error U_C/C bounds the normalized flowrate difference $\Delta\dot{m}$. Additionally, U_C/C is always four-times greater than the reference flowmeter, which is the standard minimum error defined by ANSI/NCSLZ540.3. Therefore, the F-STAr EMFM is estimated to have an error of 8% between 0.16-kg/s and 0.4-kg/s, and an error of 4% between 0.4-kg/s and 0.94-kg/s.

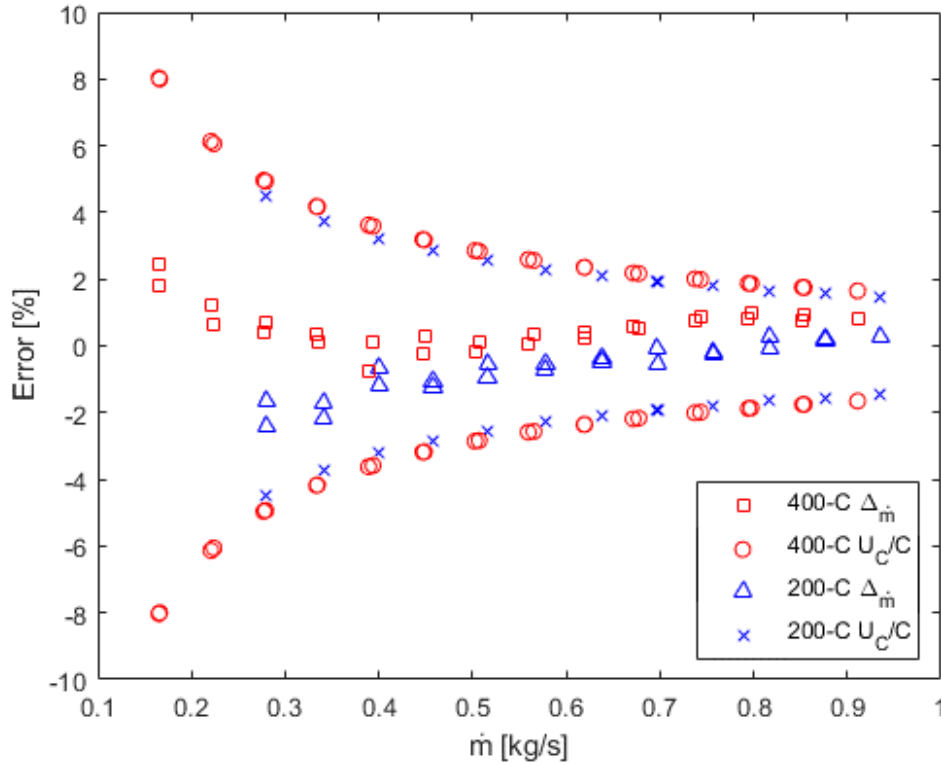


Figure 29 – Estimated F-STAr EMFM error at 200-C and 400-C. Note that the calculated difference between the F-STAr EMFM and reference flowmeter is bounded by the theoretically calculated calibration coefficient error.

$$\Delta\dot{m} = \frac{\dot{m} - \dot{m}_{\text{ref}}}{\dot{m}_{\text{ref}}} \cdot 100 \text{ [%]}$$

Equation 15

6 Conclusions and Path Forward

In summary, all F-STAr components have been manufactured, delivered, and inspected. The test article was mocked-up on the 28-inch A-Frame to verify the fit and form of each component. After this check, some minor modifications were made to a few components. Additionally, the power distribution enclosure, data acquisition and control enclosure, and programming were designed, constructed, and qualified. With the enclosures and programming completed, water qualification testing began. Initial testing showed that the measured flowrate in the current water configuration is below the desired 120-GPM flowrate. However, it was also noted that the water setup has significantly higher pressure losses than the sodium setup. In addition to the lower flowrates than desired, the pump was also observed to have excessive vibrations above 50% full rotational speed. This limited the extent of water qualification testing, and the full performance of the pump could not be measured directly. Rather it was inferred through extrapolation of the measured data.

Additionally, F-STAr's submersible flowmeter was constructed and calibrated in liquid sodium. The calibration was completed at an outside contractor's sodium loop using a NIST traceable reference flowmeter over a volumetric flow range of 3.5-GPM to 18-GPM at 200-C and 400-C. An uncertainty analysis was completed to estimate the flowmeter uncertainty. From this analysis, it was estimated that the flowmeter has an accuracy of 8% between 0.16-kg/s and 0.4-kg/s, and 4% between 0.4-kg/s and 0.94-kg/s.

Moving forward, more work will be completed to address issues that came up during the initial qualification testing with the goal of finishing the qualification of F-STAr in early FY24 followed by insertion into METL. Future work includes:

- Improve flowmeter uncertainty analysis to provide a better estimate of its measurement accuracy.
- Reduce pump vibration magnitude or constrain vibrations to resonance moves that can be avoided. To pinpoint the origin of the vibrations, the pump will be partially disassembled and operated.
- Measure the actual pump performance by simplifying the water setup and adding a valve.
- Investigate methods of increasing pump flowrate performance.
- Complete additional water testing of F-STAr in the flow sensor configuration.
- Construct a multi-physics model of the F-STAr EMFM and use calibration data as a reference. Then, use the multi-physics model to extrapolate the EMFM calibration curve.
- Weld EMFM into F-STAr piping system.
- Clean F-STAr components and reassemble for insertion into METL test vessel.
- Install F-STAr into METL Test Vessel #3.

7 Acknowledgements

The authors would like to acknowledge METL team member Daniel Andujar for all the hard work and dedication to constructing, maintaining, and operating the facility. This work is funded by the U.S. Department of Energy Office of Nuclear Energy's Advanced Reactor Technologies (ART) program. A special acknowledgement of thanks goes to Ms. Kaatrin Abbott, Fast Reactor Program Manager for the DOE-NE ART program, Dr. Bo Feng, the National Technical Director for Fast Reactors for the DOE-NE ART program, and to Mr. Bradley Tomer, Acting National Technical Director for the National Reactor Innovation Center for their consistent support of the Mechanisms Engineering Test Loop and its associated experiments, including F-STAr.

8 References

- [1] M. El-Wakil, Nuclear Energy Conversion, Scranton, Pennsylvania: Intext Education Publishers, 1971, p. 330.
- [2] Argonne National Laboratory, "Advanced Burner Reactor 1000 MWth Reference Concept," Lemont, 2007, ANL-AFCI-202.
- [3] Argonne National Laboratory, "Advanced Fast Reactor - 100 (AFR-100) Report for the Technical Review Panel," Lemont, 2014, ANL-ARC-288.
- [4] GE Nuclear Energy, "ALMR Summary Plant Design Description," San Jose, 1993.
- [5] Argonne National Laboratory, "FASTER Test Reactor Preconceptual Design Report," Lemont, 2016, ANL-ART-86.
- [6] General Electric, "PRISM Preliminary Safety Information Document," San Jose, 1987.
- [7] IAEA, "Fast Reactor Database 2006 Update," IAEA, Vienna, 2006.
- [8] J. Rein, M. Weathered, E. Kent, D. Kultgen and C. Grandy, "Flow-Sensor Test Article (F-STAr) - Design and Fabrication Status Report," Argonne National Laboratory, Lemont, 2022, ANL-ART-255/ANL-METL-40.
- [9] J. Rein, M. Weathered, E. Kent, D. Kultgen and C. Grandy, "Flow Sensor Test Article (F-STAr) - Status Report for FY2021," Argonne National Laboratory, Lemont, 2021, ANL-ART-239/ANL-METL-34.
- [10] W. Weathered, D. Kultgen, E. Kent, C. Grandy, T. Sumner, A. Moiseyev and T. Kim, "Thermal Hydraulic Experimental Test Article - Status Report FY2020," Argonne National Laboratory, Lemont, 2020, ANL-ART-211/ANL-METL-25.
- [11] H. Elrod and R. Fouse, "An investigation of electromagnet flowmeters," *Transactions of the American Society of Mechanical Engineers*, vol. 74, 1952.
- [12] W. Gray, "Magnetic Flowmeter Calibration Results (KAPL-613)," 1951.
- [13] J. Shercliff, The Theory of Electromagnetic Flow-Measurement, Cambridge University Press, 1962.
- [14] W. C. Gray and E. Astley, "Liquid metal magnetic flowmeters," *Journal of the Instrument Society of America*, vol. 1, pp. 15-23, 1954.
- [15] J. Mausteller, F. Tepper and S. Rodgers, Alkali Metal Handling and Systems Operating Techniques, Gordon and Breach, 1968.
- [16] U. A. E. Commission, "Permanent Magnet Flowmeter for Liquid Metal Piping Systems (Technical Report RDT C 4-5T)," 1971.
- [17] L. G. Vasil'yev and A. I. Kozhainov, "Magnetohydrodynamics in Marine Engineering," 1967.
- [18] S. Kim and C. Dooze, "Temperature compensation of NdFeB permanent magnets," 1998.
- [19] M. Weathered, C. Grandy, M. Anderson and D. Lisowski, "High Temperature Sodium Submersible Flowmeter Design and Analysis," *IEEE Sensors Journal*, vol. 21, no. 15, pp. 16529-16537, 2021.
- [20] J. Fink, "A Consistent Assessment of the Thermophysical Properties of Sodium," *High Temperature Materials Science*, vol. 36, pp. 65-104, 1996.
- [21] J. 100:2008, "Evaluation of measurement data - Guide to the expression of uncertainty in measurement," JCGM, 2008.
- [22] P. Kirillov, V. Kolesnikov, V. Kuznetsov and N. Turchin, "Instrument for Measuring the Pressure, Flow, and Level of Fused Alkali Metals," *Atomic Energy (USSR)*, vol. 9, no. 3, pp. 173-181, 1960.



Nuclear Science and Engineering Division

Argonne National Laboratory

9700 South Cass Avenue

Lemont, IL 60439

www.anl.gov



Argonne National Laboratory is a U.S. Department of Energy
laboratory managed by UChicago Argonne, LLC